ChemComm

FEATURE ARTICLE

View Article Online
View Journal | View Issue

Cite this: *Chem. Commun.*, 2026, **62**, 6830

Non-thermal plasma restructuring of electrocatalyst surfaces for efficient hydrogen and oxygen reactions

Chu Qin, [a] Zhenglong Tao, [a] Xuanhao Wu *[b] and Zhongqing Jiang *[a]

Received 30th November 2025,
Accepted 9th March 2026

DOI: 10.1039/d5cc06818e

rsc.li/chemcomm

Electrocatalysts for water electrolysis, fuel cells, and metal–air batteries are largely governed by processes occurring within the outermost few nanometres of their surface. Low-temperature plasmas provide an effective means to tailor this region, using energetic electrons and reactive species to enable rapid, surface-confined modification while preserving the underlying scaffold. In this Feature Article, we review plasma engineering strategies for HER, OER and ORR electrocatalysts, including examples from zinc–air batteries and direct methanol fuel cells. We classify plasma effects into five generic design modes: phase transformation and plasma-assisted derivation; defect and vacancy engineering; plasma-induced doping; plasma-enabled deposition and interface construction; and single-atom anchoring with strong metal–support interactions. We also propose simple design rules that connect controllable plasma parameters to targeted active sites and device-level performance.

1. Introduction

Electrochemical energy technologies, including water electrolysis, hydrogen production, fuel cells, and metal–air batteries, critically depend on catalysts that can drive the hydrogen evolution (HER), oxygen evolution (OER), and oxygen reduction (ORR) reactions with high activity, durability, and efficient use of precious metals. Despite rapid progress, sluggish multi-electron kinetics and instability under industrially relevant conditions still constrain device performance and cost. In this context, plasma-assisted nanocatalyst engineering has emerged as a practical interface-engineering tool to tailor active phases, interfaces, and defect chemistries under comparatively mild conditions.[9,10]

Low-temperature plasmas provide a non-equilibrium environment, in which energetic electrons generate a dense flux of radicals, ions and excited species while the heavy species remain comparatively cool. Here, "low-temperature" is used in the plasma-physics sense to denote non-thermal, non-equilibrium discharges, where electron-driven chemistry proceeds while the heavy species remain far cooler than in thermal plasmas.[11,12] Under these conditions, conversion is confined to a shallow "skin" (few-tens of nanometers), so a parent scaffold

[a] *Zhejiang Key Laboratory of Quantum State Control and Optical Field Manipulation, Department of Physics, Zhejiang Sci-Tech University, Hangzhou 310018, China. E-mail: zhongqingjiang@zstu.edu.cn*
[b] *State Key Laboratory of Soil Pollution Control and Safety, Zhejiang University, Hangzhou 310058, China. E-mail: xuanhao.wu@zju.edu.cn*

Chu Qin

Chu Qin received her BS degree in Chemistry from Wuhan University in 2015 and her PhD degree in Chemistry from Washington University in St. Louis in 2020. She has been an Assistant Professor in the Department of Physics at Zhejiang Sci-Tech University since 2021. Her research focuses on low-temperature plasma-assisted synthesis and modification of chalcogenide-based electrodes for electrocatalysis and energy storage applications.

Zhenglong Tao

Zhenglong Tao is a second-year graduate student in the Physics Department at Zhejiang Sci-Tech University. Under the supervision of Prof. Zhongqing Jiang, his research centers on leveraging electrospinning technology to synthesize nanofiber-based materials for energy storage applications.

can be chemically recast at the surface without losing its architecture.[20] For electrocatalysts, this ''skin-depth'' conversion is advantageous: the outermost atomic layers control adsorption and reaction barriers, while the unconverted bulk maintains mechanical integrity, electrical percolation, and open porosity. With short treatments often in the range of seconds to minutes, the plasma exposure can simultaneously induce reduction/oxidation, etching, doping, and thin-film growth, offering a versatile and tunable approach for catalyst construction.[25–28]

The practical value of this approach shows up across hydrogen and oxygen electrodes. For HER, converting oxide or hydroxide precursors to thin metallic-like phosphide skins (or to nitride skins with high carrier density) lowers the energy cost of water dissociation and tunes ΔG_{H^*} toward the optimal range.[30,31] For OER and ORR, vacancy-rich chalcogenide or sub-oxide layers adjust the binding energy of OOH*/OH*/O* intermediates, while adjacent nitride or metallic regions provide fast electron delivery and help stabilize the working oxidation states during potential swings.[35] In overall water splitting, pairing these two functions on a common 3D current collector (carbon cloth, foams, MOF-derived carbons) reduces ohmic losses and improves durability at high current densities.[36] In Zn–air batteries and direct methanol fuel cells, conformal plasma-grown skins help maintain activity under cycling, fuel crossover, and carbonation.[37–39]

Several characteristics of low-temperature plasmas make these outcomes reproducible and tunable. First, the time-temperature leverage: non-equilibrium chemistry opens reaction paths, so phase conversion, anion incorporation, and gentle reduction finish quickly and at low gas temperature. Second, depth control: because the reaction front is self-limited by short radical lifetimes and slow solid-state diffusion at low temperature, conversions stop naturally after a few nanometers, yielding thin and uniform shells on complex 3D supports. Third, fast anion exchange and near-surface redox produce non-stoichiometry (oxygen/chalcogen vacancies) and mixed valence, and the shallow conversion maximizes the density of phase boundaries, which often raise intrinsic activity and improve charge transfer when kept within a narrow thickness window.

Plasma processing also offers a set of controllable parameters that map directly onto catalytic requirements. The feed gas governs the dominant surface chemistry. For example, O_2 for oxidation and oxygen-vacancy tuning,[40] H_2/NH_3 for reduction and nitridation,[41] PH_3 or organophosphorus vapors for phosphidation,[42] and S/Se-containing feeds for chalcogenization.[43] Applied power, duty cycle and treatment time determine the radical flux and thus the depth of conversion, while pressure and flow rate control mean free paths and residence times, which in turn dictate how conformally porous scaffolds are modified.[44] In capacitively coupled plasmas (*e.g.* atmospheric-pressure plasma jets, dielectric-barrier discharges, or low-pressure RF/ICP reactors), applying a substrate bias allows the ion bombardment energy to be tuned, providing an additional handle over surface activation and defect generation. In practice, a sequence of short, mild plasma exposures often outperforms a single aggressive treatment, producing thinner shells with higher interfacial area and fewer blocked pores, while minimizing stress and particle growth.

A large body of literature documents the promise of plasmas across energy chemistries (*e.g.*, hydrogen production, ammonia synthesis, and broader plasma catalysis), but most surveys are organized by application or by reactor chemistry. This can obscure the fact that the same plasma effect (*e.g.*, phosphidation or N-doping) is portable across materials families and reactions, and that performance gains often trace back to a small number of recurring structural motifs, like phase conversion, vacancies, heterointerfaces, and metal–support interaction (MSI). What is needed, therefore, is a clear link between tunable plasma parameters, the structural changes they produce, and the resulting catalytic behavior (as shown in Table 1), so that insights can be transferred across different systems.

Building on our group's sustained work with plasma-engineered electrocatalysts spanning HER, OER, ORR, zinc–air batteries (ZABs), and direct methanol fuel cells (DMFC)

Xuanhao Wu

Xuanhao Wu is a Hundred-Talent Assistant Professor at the School of Environmental and Resources, Zhejiang University. He received his BS from Fudan University and PhD from Washington University in St. Louis, followed by postdoctoral training at Yale University. His research focuses on environmental catalysis, mainly developing electro-/photo-/thermo-catalysts and systems for the conversion and resource recovery of nitrogenous pollutants and greenhouse gases.

Zhongqing Jiang

Zhongqing Jiang is a professor in Department of Physics at Zhejiang Sci-Tech University. Dr Jiang received his PhD in 2010 in Plasma Physics at Institute of Plasma Physics, Chinese Academy of Sciences. He was a Postdoctoral Fellow at the University of Texas at Austin in 2011–2013. His research interests include synthesis and modification of electrode materials and polymer electrolyte membrane by low temperature plasma for applications in fuel cells, all-solid-state Li metal batteries, zinc air batteries and sodium ion batteries, etc.

Table 1 Plasma parameters and catalytic metrics

Reference	Plasma parameters	Structural descriptor	Catalytic metric
Li *et al.*[45]	RF glow discharge N_2/H_2, N_2/H_2 = 40 : 1; 24 Pa; RF power 120 W; 1 h; 250 °C	$Ni(OH)_2$ → porous Ni_3N while keeping nanosheet macrostructure; Ni–N hybridized states	HER: η = 44 mV, Tafel = 46 mV dec^{-1}
Xu *et al.*[1]	Ar/NH_3 RF plasma; 20 Pa; 100 W; 500 °C; 1 h	Se-vacancy EPR $g \approx 2.003$; Raman I_D/I_G 0.87 (plasma) *vs.* 0.79; BET 46.1 vs 18.4 $m^2\ g^{-1}$	OERR $E_{1/2}$ = 0.80 V; OER η = 311 mV@30 mA cm^{-2}
Wei *et al.*[48]	H_2/N_2 RF plasma; $H_2 : N_2$ = 1 : 1; 20 sccm; 30 Pa; 200 W; 1 h	Surface Ni_3N/Mo_2N heterostructure on nanorods; crystalline shell (~12 nm) over amorphous core; EPR g = 2.31	HER: η_{100} = 66 mV; η_{500} = 134 mV; Tafel = 38 mV dec^{-1}
Ouyang *et al.*[14]	RF N_2 plasma; 13.56 MHz; 500 W; N_2 40 sccm; ~30 Pa; 300 s	Ni plate → Ni_3N nano-framework; facet control: dominant (2–10) (cooling plasma) *vs.* (2–11) (normal plasma)	HER: η_{10} = 58 mV; η_{100} = 183 mV; Tafel = 64 mV dec^{-1}; stable 72 h@−0.4 V *vs.* RHE
Zha *et al.*[3]	RF N_2 plasma; 100 W; 20 Pa; N_2 5 sccm; phosphorization at 300 °C, 90 min	Ni-Doped CoP_3 NPs on N-doped carbon nanofibers; rich P vacancies (g = 2.003); BET 44.4 $m^2\ g^{-1}$ (*vs.* 20.6 $m^2\ g^{-1}$ thermal)	HER: η_{100} = 107 mV, Tafel 68 mV dec^{-1}; OER: η_{100} = 306 mV, Tafel 97 mV dec^{-1}
Salem *et al.*[15]	RF-PECVD PH_3/Ar plasma; PH_3/Ar = 1 : 99; 10 sccm; 980 mTorr; 100 W; 250 °C; 3 h	MnNiCoP nanoflowers on NF; Ni–P/Co–P formation	HER: η_{10} = 14 mV, Tafel = 58 mV dec^{-1}; OER: η_{10} = 289 mV; overall: 1.48 V@10 mA cm^{-2}
Xu *et al.*[2]	Ar RF plasma (commercial 13.56 MHz); 100 W; 40 Pa; 120 s (0–240 s tested)	BET area 160.26 *vs.* 95.27 $m^2\ g^{-1}$ (engraved *vs.* pristine); surface Co^{2+}/Co^{3+} ratio 1.2 *vs.* 1.0	OER: η_{10} = 0.30 V; Tafel 68 mV dec^{-1}; TOF 0.21 s^{-1}@η = 0.3 V
Han *et al.*[17]	Ar or O_2 plasma; 100 W; 130 Pa; 240 s	O vacancy ratio (A/B): 0.48 (L), 0.70 (P), 1.60 (H)	CO_2RR: FE(CO) 94.8% at −0.62 V vs RHE; Tafel 77 mV dec^{-1}
Ye *et al.*[21]	O_2 RF plasma; 100 W; 20 Pa; 20 min	Co/CoO heterojunction with abundant oxygen vacancies; EPR signal present; ECSA 351.75 cm^2 (*vs.* 247.25 cm^2 without plasma)	ORR $E_{1/2}$ = 0.855 V; OER 1.607 V@10 mA cm^{-2}; ΔE 0.752 V; liquid ZAB 133.5 mW cm^{-2}, 1000 cycles
Wang *et al.*[6]	Ar plasma, 18 W, 0.6 Torr	Exposure of $PtSe_2$ (101) facet (60 s); Se loss; formation of Pt-rich amorphous layer	17.6 mA cm^{-2} (60 s, 50 mV s^{-1}); Tafel slope: 177 mV dec^{-1}
Zhang *et al.*[13]	Ar microwave plasma, 100 W, 0.5–1.0 Pa, 15–45 min	Defect-engineered CoP_3/Ni_2P heterostructure (vacancy-type/O-refilling defects at interface)	HER: η_{10} = 21 mV (acidic), 37 mV (alkaline); OER: η_{10} = 300 mV
Li *et al.*[4]	NH_4F RF plasma, 500 W and 13.56 MHz for 1 min	Dual N, F incorporation in Co_3O_4, increased M–O covalency; O 2p upshift; lattice-oxygen activation	OER: η_{10} = 254 mV
Zheng *et al.*[58]	DBD cold plasma; 100 V, 1.5 A; 30 min; gases: Ar, O_2, air; T < 140 °C	Oxygen vacancies; Co^{3+} → Co^{2+} partial reduction; surface CoO formation; N doping up to 10.1 at%	ORR onset shift +0.03 V; j = 4.9 mA cm^{-2} at 0.2 V (*vs.* RHE); e^- transfer number ≈ 3.99
Chen *et al.*[19]	Focused plasma jet system with AC power: 0–30 kV, 8.00–30.0 kHz	Electrode-emerged $NiCo(OH)_x/NiCo_2O_4$ nanointerfaces grown directly on Ni foam	At j = 100 mA cm^{-2}: HER η = 306 mV, OER η = 484 mV
Hoek *et al.*[68]	O_2 plasma steps; RF power 200 W; 0.1 Torr	Ultrathin NiO_x@Co_3O_4 (amorphous/defect-rich NiO_x shell)	OER: η_{10} = 360 mV (*vs.* 420 mV for Co_3O_4/CC)
Zhu *et al.*[22]	H_2/N_2 plasma; 200 W; 80 mL min^{-1}; 20 min	Defective TiO_2 nanowires (oxygen vacancies); ultrafine Ir nanoparticles; Sr single atoms stabilized on defective TiO_2	OER: η_{10} = 250 mV; HER: η_{10} = 32 mV

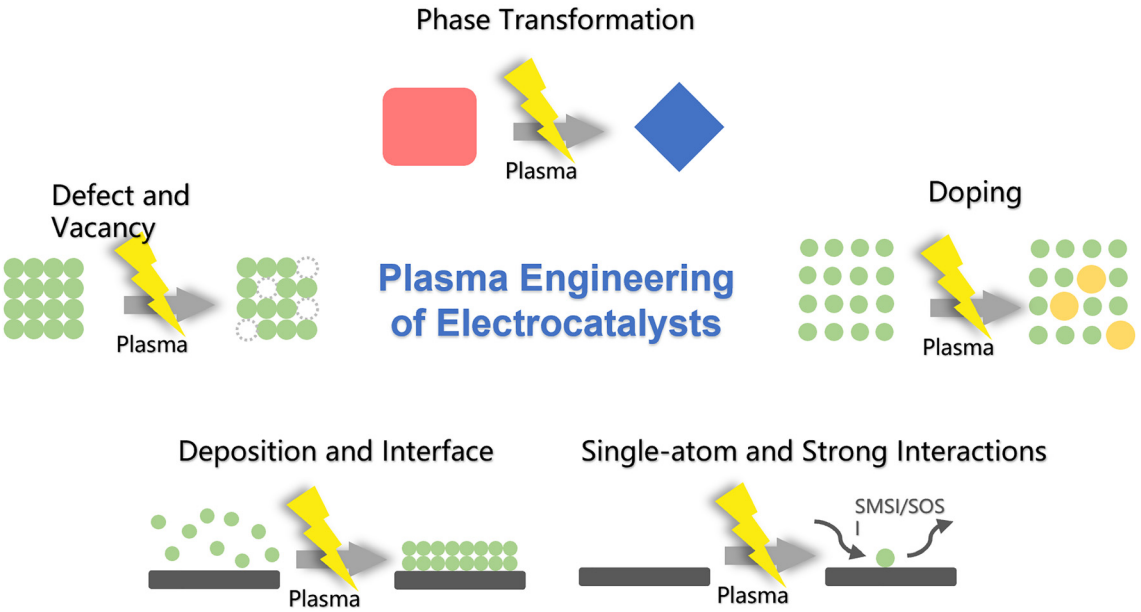

Fig. 1 Schematic overview of plasma-enabled design modes for electrocatalysts.

cathodes, we frame plasma's role through five fundamental effect categories (Fig. 1): (i) phase transformation and plasma-assisted derivation; (ii) defect and vacancy engineering; (iii) plasma-induced doping; (iv) plasma-enabled deposition and interface construction; (v) single-atom anchoring and strong metal–support interactions. Across HER, OER, ORR, overall water splitting, ZABs, and DMFCs, the recurring theme is the same: write the chemistry where the reaction happens and keep the physics that carries current. Low-temperature plasmas make that balance practical, scalable, and compatible with binder-free electrodes and device-level current densities.

For each effect, we describe how plasma parameters drive structural evolution, and how these structures in turn modulate *in situ* binding and transport to deliver device-level advantages. By emphasizing a structure-first causality that links controllable plasma conditions to characteristic structural signatures and then to catalytic performance, we aim to provide portable design rules that can be applied across HER, OER and ORR systems rather than treating each application in isolation. This mechanism-oriented view is intended to complement application-focused reviews and to guide predictive, scalable catalyst design that leverages the distinctive capabilities of non-thermal plasmas.

2. Plasma effects in catalyst engineering

2.1. Phase transformation and derivation

Phase transformation is among the most fundamental yet effective plasma-induced effects for tailoring catalytic materials. This section covers cases where plasma produces a discernible near surface phase or conversion layer, evidenced by new phase signatures such as XRD or SAED, or a clearly resolved shell. Compared with conventional thermal conversion routes, non-thermal plasma enables phase transformation to be confined to the near-surface region. Non-thermal electrons, radicals and ions drive rapid, near-surface anion exchange and lattice rearrangement, which enables chemically intensive transformations of the active phase, including conversion into nitrides, phosphides, sulfides, selenides or defect-rich oxides. Two features are particularly important for electrocatalysis: the emergence of a new surface phase and the formation of closely coupled phase boundaries with distinct electronic structures. Together, these reshape adsorption energetics at the active surface while ensuring efficient mass and electron transport through the electrode.

Plasma nitridation provides one of the clearest demonstrations of this decoupling between surface chemical change and retaining architectures. As reported by Li *et al.*, $Ni(OH)_2$ nanosheets were converted into porous Ni_3N under an N_2/H_2 radio-frequency (RF) glow-discharge plasma, which was chosen for its non-thermal, radical-rich environment that enables rapid nitridation while preserving the nanosheet framework.[45] In this discharge, adding H_2 promotes the formation of NH* species and simultaneously assists the reduction of $Ni(OH)_2$ to reactive Ni, together accelerating Ni–N bond formation and the $Ni(OH)_2 \rightarrow Ni_3N$ transformation. Replacing OH^- with N^{3-} strengthens metal–ligand covalency and introduces Ni–N hybridized states near the Fermi level, which manifests as lower charge-transfer resistance and enhanced HER kinetics. Liu *et al.* showed that NiCoO nanostructures exposed to N_2 plasma develop NiCoN-rich shells surrounding NiCoO cores.[46] The resulting oxide–nitride junctions create internal electric fields arising from the electronegativity contrast between N and O and the coexistence of multiple Ni/Co valence states, effectively lowering the barriers for OH^- adsorption and deprotonation in zinc–air ORR/OER cycles.

Building on this observation, Xu *et al.* extended the plasma-induced phase-transformation concept to chalcogenides.[1] They first prepare Ni/NCNT@CC by electrodeposition, then obtain

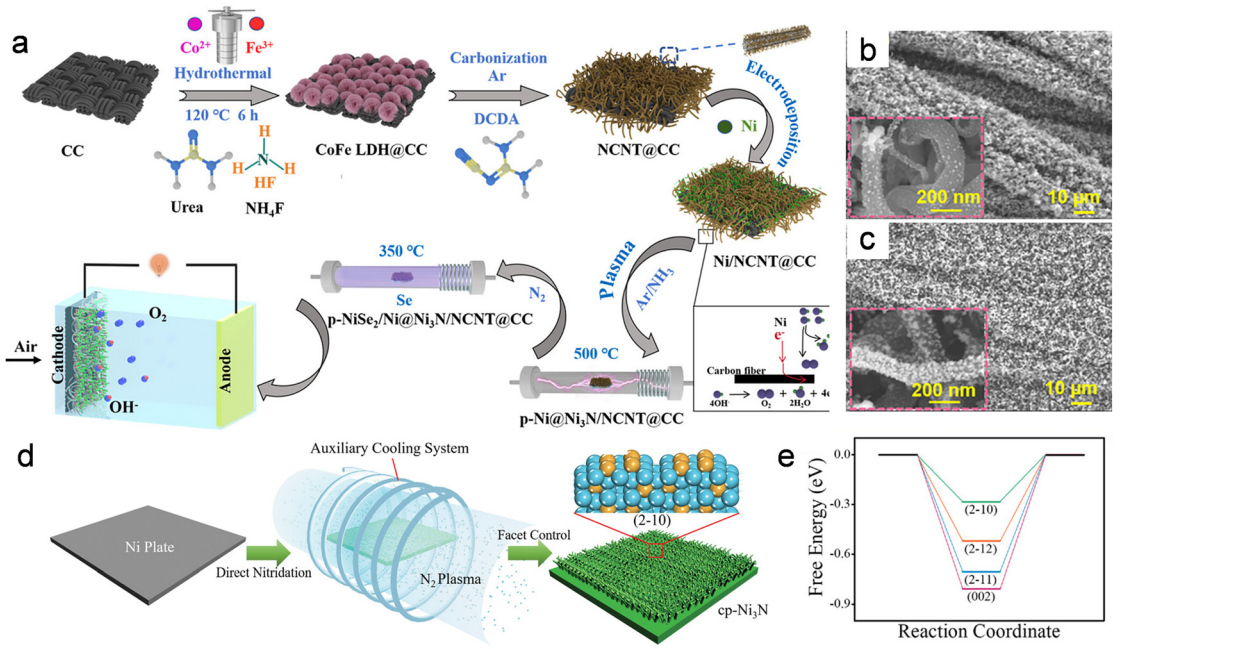

Fig. 2 (a) Schematic illustration of the synthetic process of the p-$NiSe_2$/Ni@Ni_3N/NCNT@CC. SEM images of (b) p-Ni@Ni_3N/NCNT@CC and (c) p-$NiSe_2$/Ni@Ni_3N/NCNT@CC. Reproduced with permission.[1] Copyright 2025, Wiley-VCH. (d) Schematic Illustration of the as-prepared Ni_3N nano-frameworks through cooling-assisted plasma process. (e) Free energy for HER on typical facets of hexagonal Ni_3N model. Reproduced with permission.[14] Copyright 2022, Wiley-VCH.

p-Ni@Ni_3N/NCNT@CC by Ar/NH_3 RF plasma nitridation, a configuration typically chosen to provide a high flux of reactive nitrogen/hydrogen species for rapid, near-surface nitride formation without collapsing the porous carbon scaffold. Subsequent high-temperature selenization produces a ternary p-$NiSe_2$/Ni@Ni_3N/NCNT@CC catalyst in which $NiSe_2$/Ni-Ni_3N heterojunctions are uniformly anchored on N-doped CNTs (Fig. 2a–c). In the RF Ar/NH_3 discharge, the interfacial nitridation is governed by plasma-generated NH* (and related NH_x*) species together with Ar* activation/etching, which promotes Ni–N bond formation and stabilizes a thin Ni_3N skin and nitrogen-enriched interface that survives the subsequent high-temperature selenization. These multiple heterointerfaces generate band offsets that redistribute charge across the junctions, thereby optimizing both H_2O activation and H* binding relative to any single phase. Liu *et al.* further showed that nitridation of $NiCo_2S_4$ generates a $NiCo_2S_4$@Co_2N heterostructure, producing sulfide–nitride boundaries populated with coordinatively unsaturated metal sites that facilitate water dissociation.[47]

Likewise, Wei *et al.* showed that near-room-temperature H_2/N_2 plasma converts Ni–Mo oxide hydrate nanorods into a conformal Ni_3N/Mo_2N shell, where reactive H species first promote reduction and Mo–O/Ni–O bond breaking, followed by activated N species permeation to form M–N bonds.[48] The resulting nitride–oxide heterostructure lowers the barrier for nitride formation and couples Ni_3N sites for H adsorption with Mo_2N sites for water activation, thus enhancing alkaline HER. At higher plasma reactivity, non-thermal nitridation can even steer crystallographic outcomes: Ouyang *et al.* reports that a cooling-assisted plasma process suppresses surface heating and thereby enables preferential exposure of the metastable Ni_3N(2–10) facet rather than the thermodynamically favored (2–11) facet.[14] Notably, this was achieved in a RF nitridation plasma, where auxiliary cooling tunes the plasma-surface energy coupling instead of changing the precursor or reaction chemistry. Operando plasma diagnostics further show that cooling reduces surface temperature and moderates key plasma parameters, shifting the nitridation regime away from thermally stabilized growth and toward metastable facet exposure. DFT further identifies Ni_3N(2–10) as having a nearly optimal ΔG_{H^*} for alkaline HER, explaining the superior kinetics observed experimentally (Fig. 2d and e). Collectively, these studies show that plasma nitridation rewires the surface electronic structure by introducing more metallic d–p hybrid bands, internal fields and fast charge-transfer channels, while leaving the micron-scale geometry effectively untouched.

On the same principle of surface-confined anion exchange, plasma phosphidation converts hydroxide, oxide and chalcogenide precursors into interfacially rich phosphides whose electronic properties differ markedly from their parent phases. In our recent work, Zha *et al.* showed that with NaH_2PO_2 and RF plasma, the sheet-like NiCo LDH collapses into intertwined nanowires composed of Ni-doped CoP_3 nanoparticles uniformly anchored on N-doped carbon nanotube frameworks[3] (Fig. 3a and b). This low-pressure N_2 RF discharge was selected to supply a high flux of reactive P-containing species from NaH_2PO_2 decomposition while limiting bulk heating, enabling a rapid, surface-confined phosphidation that preserves the conductive carbon backbone. Mechanistically, the dominant plasma effect is the generation of energetic radicals/ions that

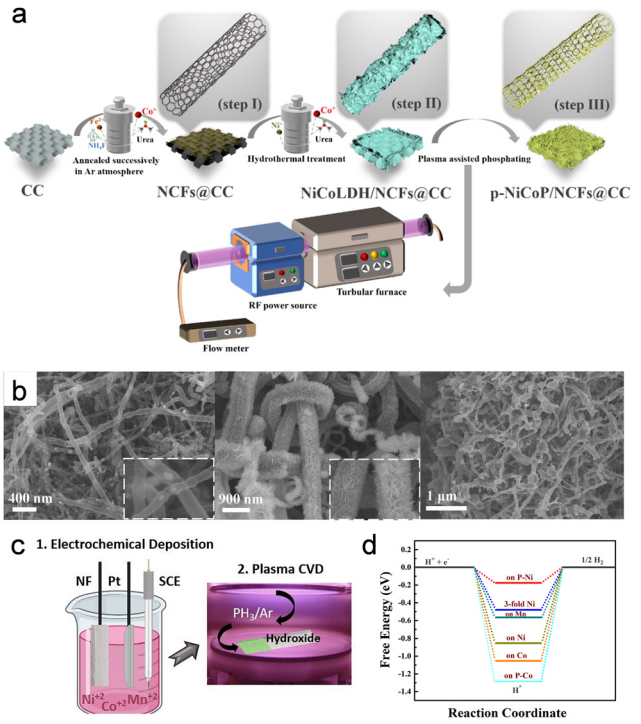

Fig. 3 (a) Schematic of the synthesis process of the p-NiCoP/NCFs@CC. (b) SEM images of NCFs@CC, NiCoLDH/NCFs@CC, and p-NiCoP/NCFs@CC. Reproduced under the terms of CC-BY 4.0 license.[3] (c) Schematic of the design of the MnNiCoP alloy on nickel foam as electrolytic water splitting bifunctional catalyst. (d) Free-energy diagram of intermediate state for H* adsorption on the MnNiCoP (0001) surface. Reproduced with permission.[15] Copyright 2023, Wiley-VCH.

accelerate M–O(H) bond rupture and M–P bond formation, while concurrent plasma etching promotes P-defect formation and surface roughening, which collectively enhance charge transfer and accelerating H*/OH* adsorption at the phosphide surface.

Plasma phosphidation can push MoS_2-based hybrids into more strongly coupled metal–phosphide junctions, rather than simply completing an anion-exchange step. Fu *et al.* used RF plasma-assisted phosphorization to synthesize MoS_2@$Ni_{12}P_5$/ZnP_2, where finer $Ni_{12}P_5$ and ZnP_2 nanocrystallites uniformly decorate MoS_2 and create dense nanoscale heterojunctions with strengthened electronic coupling.[49] Zhang *et al.* reported that plasma-assisted phosphidation transforms $NiMoO_4$ nanorods into a tri-phase MoP_2/Ni_3P/MoO_2 composite composed of small sub-nanometer crystallites embedded within the preserved rod architecture.[50] In this discharge, energetic N/N_2^+ species promote the generation of reactive PH· and H· from NaH_2PO_2-derived PH_3, accelerating phosphidation and simultaneously enriching oxygen vacancies in MoO_2.

As reported by Salem *et al.*, ternary Mn–Ni–Co hydroxides phosphidized using a PH_3 plasmas (plasma-enhanced chemical vapor deposition, PECVD) process, yielding porous flower-like MnNiCoP that retains the hierarchical framework while shifting from a hydroxide-like, weakly conductive state to a more metallic phosphide surface[15] (Fig. 3c and d) The key plasma contribution is the high flux of reactive species that accelerates M–O(H) bond removal and M–P bond formation with uniform phosphidation across the 3D architecture, thereby improving conductivity and exposing dense catalytic sites for fast alkaline HER/OER kinetics.

Plasma phosphidation can be paired with prior plasma oxidation to stack phases with complementary roles. Zhang *et al.* created $VNiCoP_y$/$NiFeO_x$ heterostructures by using an O_2 atmospheric-pressure plasma jet (APPJ) to form vacancy-rich $NiFeO_x$, followed by plasma-assisted phosphating of the overlying VNiCo layer.[51] The resulting phosphide/oxide junction shows interfacial charge redistribution, where the phosphide supplies conductive pathways and the oxide stabilizes high-valent states; importantly, the plasma steps preserve the 3D architecture while tightening interfacial coupling.

Plasma-assisted oxidation and oxide deposition offer a third pathway to surface phase engineering, particularly for ultrathin catalytic layers and dynamic reconstruction. As reported by Mallmann *et al.*, atmospheric-pressure plasma-enhanced CVD is used to produce Co_3O_4 films at reduced substrate temperatures, where the plasma provides reactive oxygen-containing species and simultaneously promotes rapid nucleation and controlled crystallization.[52] In this AP-PECVD setup, the blown-arc plasma torch produces a reactive afterglow in which long-lived oxygen-containing radicals (notably NO and OH) dominate precursor activation and oxide growth. Yang *et al.* showed that O_2 plasma pretreatment combined with plasma-enhanced ALD yields NiO_x@Co_3O_4 electrodes with an ultrathin amorphous NiO_x shell, where an RF O_2 plasma step supplies O species for surface activation and the PE-ALD plasma pulse enables low-temperature, conformal oxidation during growth.[53] XPS reveals abundant Ni^{3+} and non-lattice oxygen, indicating a defect-rich sub-oxide that can dynamically reconstruct into Ni(oxy)hydroxide during OER operation. In all of these cases, the oxide phase formed by plasma is electronically and structurally primed for further transformation under operation, lowering the barrier to reconstruct into catalytically competent (oxy)hydroxide states.

Taken together, these nitridation, phosphidation and oxidation studies point to a unified mechanism. Non-thermal plasmas selectively rewrite the chemistry and electronic structure of the outer reaction layer, generating new phases, heterointerfaces and defect configurations that govern intermediate binding and reaction kinetics, while the mesoscopic scaffold remains largely unchanged and continues to support efficient electron and mass transport. Across systems, SEM and low-magnification TEM consistently reveal inherited nanosheet, nanorod, nanoarray and foam morphologies, even as HRTEM and XPS uncover thin transformed shells enriched in nitride, phosphide or sub-oxide species, modified metal valence states and redistributed charge densities. A conceptual workflow that begins with LDH, oxide or chalcogenide precursors, proceeds through a radical- and electron-rich plasma environment, and emerges as multi-phase, interface-dense electrocatalysts captures the essence of these transformations. The recurrence of these plasma-driven motifs across alkaline water splitting, overall electrolysis, zinc–air batteries and fuel-related reactions

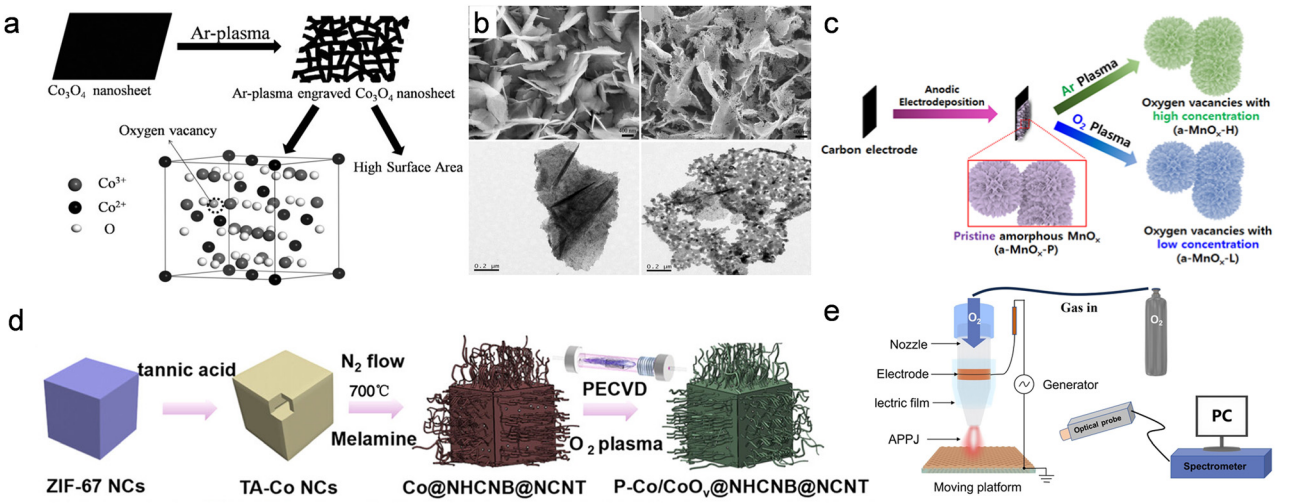

Fig. 4 (a) Fabrication of oxygen-vacancy-rich Co_3O_4 with high surface area *via* Ar plasma engraving. (b) SEM and TEM images of pristine (left) and Ar-plasma engraved (right) Co_3O_4, respectively. Reproduced with permission.[2] Copyright 2016, Wiley-VCH. (c) Schematic of the plasma treatment for the a-MnO_x catalysts with different concentrations of oxygen vacancies. Reproduced with permission.[17] Copyright 2020, Elsevier. (d) The synthesis process of the P-Co/CoO_V@NHCNB@NCNT. Reproduced under the terms of CC-BY 4.0 license.[21] (e) Schematic illustration showing the APPJ setup and the treatment of the MnO_x film. Reproduced with permission.[32] Copyright 2024, Wiley-VCH.

underscores the versatility of non-thermal plasmas in re-engineering surface phases and electronic landscapes without compromising the advantages inherent to rational nanoarchitectural design.

2.2. Defect and vacancy engineering

Plasma-induced defect engineering represents a second, complementary axis to the phase transformations discussed above. This section focuses on situations where the parent phase is largely retained while defect populations or coordination disorder are tuned, as indicated by EPR signals, defect components in XPS, or local structure changes in EXAFS. Instead of converting the parent phase into nitrides or phosphides, non-thermal plasmas can leave the crystallographic identity and nanoarchitecture essentially unchanged while densely decorating the near-surface region with vacancies, distorted coordination environments and disordered shells. These local imperfections are highly effective in reshaping the electronic structure, tuning adsorption energetics and opening new reaction channels, yet they are confined to only a few nanometres so that the underlying scaffold continues to provide mechanical integrity and efficient electron and mass transport. In contrast to ion implantation or high-temperature reduction, which can introduce deep lattice damage, non-thermal plasma generates defects and vacancies through surface-localized chemical reactions, making it particularly suitable for engineering electrocatalytically active interfaces with minimal bulk disruption.

The clearest picture emerges from oxides in which plasma engraving generates oxygen vacancies. In a widely cited study on Co_3O_4 nanosheets by Xu *et al.*, low-power plasma bombardment roughens the sheet surfaces, removes lattice oxygen and partially reduces Co^{3+} to Co^{2+} while leaving the spinel framework intact.[2] (Fig. 4a and b) Specifically, an RF Ar plasma was used as an ion-assisted engraving/etching treatment, where energetic Ar species primarily drive surface sputtering and oxygen removal, so the resulting oxygen vacancies are largely confined to the near-surface region. XPS, EPR and EXAFS collectively show the appearance of vacancy-related oxygen components, changes in Co coordination and a more disordered Co–O environment, which together increase electronic conductivity and introduce defect states that promote lattice-oxygen mediated OER pathways.

A related strategy was adopted in amorphous MnO_x by Han *et al.*[17] (Fig. 4c). Here, controlled Ar and O_2 plasma treatments were used to tune vacancy density: Ar plasma favors oxygen removal *via* energetic-species-driven surface activation/etching, whereas O_2 plasma provides oxygen-containing reactive species that suppress or passivate V_O sites. Electrochemical CO_2 reduction on these vacancy-rich MnO_x films shows markedly higher CO faradaic efficiency and lower overpotentials, consistent with the idea that V_O sites stabilize CO_2^- and facilitate subsequent proton–electron transfer. Liang *et al.* extended this concept to crystalline WO_3 nanowires for acidic OER: a brief Ar plasma sputtering step creates a high density of surface oxygen vacancies, lowers the average W valence and distorts surface WO_6 octahedra, as seen by atomic-resolution microscopy and XAFS.[54]

Similar oxygen-defect behavior also emerges in more compositionally complex systems, including those developed in our Zn–air and OER studies. Ye *et al.* used plasma activation on Co-based air electrodes, showing that O_2-containing plasmas generate oxygen non-stoichiometry and high-valent Co species at the surface without collapsing the porous framework[21] (Fig. 4d). In their work, optical emission spectroscopy (OES) confirms the presence of energetic O species and O_2^+ in the O_2 RF plasma discharge. Mechanistically, these reactive O species partially oxidize the Co surface to form a thin CoO skin, while concurrent energetic bombardment/etching helps create

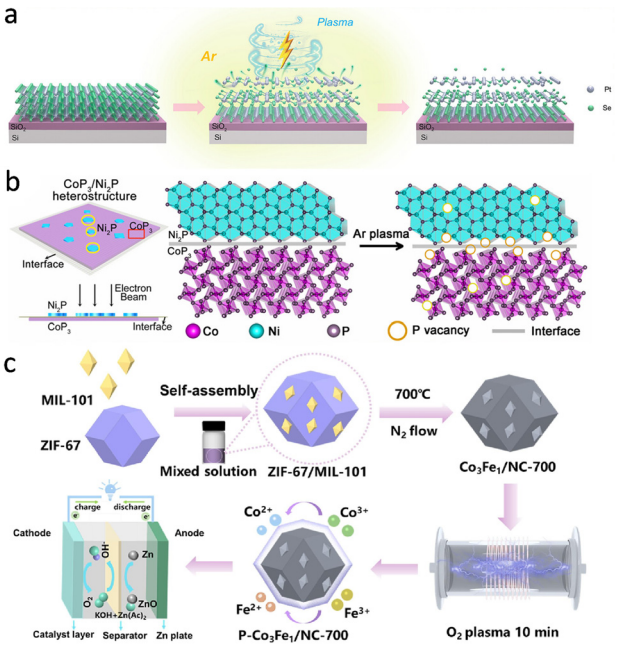

Fig. 5 (a) Schematic illustration of $PtSe_2$ nanosheet under Ar plasma treatment. Reproduced with permission.[6] Copyright 2025, Wiley-VCH. (b) Schematic illustration of the synthesis process of CoP_3/Ni_2P. Reproduced with permission.[13] Copyright 2021, Wiley-VCH. (c) Schematic illustration of the synthesis approach of P-Co_3Fe_1/NC-700. Reproduced with permission.[23] Copyright 2023, Elsevier.

oxygen-vacancy-rich Co/CoO heterojunctions. The resulting electrodes exhibit enhanced bifunctional ORR/OER activity and improved full-cell performance, with XPS and EPR fingerprints that closely mirror the V_O signatures in Co_3O_4 and MnO_x.

Zhang *et al.* pursued a related strategy in Ni-based OER catalysts, where atmospheric-pressure plasma treatments increase the fraction of high-valent metal sites and introduce disordered oxygen environments that favour rapid redox cycling under OER conditions.[55] Qin *et al.* further demonstrated that plasma-generated defective oxide skins exhibit exceptional structural and compositional stability. Post-operation analyses revealed that the catalyst, with its inherently high concentration of stabilized Mn^{3+} and oxygen vacancies, maintains its active state during the oxygen evolution reaction, directly contributing to the high activity and long-term durability[32] (Fig. 4e).

Beyond oxygen, non-thermal plasmas can also sculpt chalcogen and pnictogen vacancy landscapes. In the case of layered $PtSe_2$ crystals by Wang *et al.*, RF plasma exposure preferentially removes Se from the outermost layers, creating Se vacancies and driving partial reduction or segregation of Pt at the surface[6] (Fig. 5a). Because the feed is inert Ar, the dominant role of the plasma is ion/electron-assisted physical etching, which selectively depletes the more weakly bound chalcogen from the topmost layers and is naturally self-limited in depth. The resulting Pt-enriched, vacancy-populated skin therefore arises from a near-surface compositional "reset" rather than bulk phase conversion. Structural and spectroscopic analysis reveal a Pt-rich, defect-populated skin coherently coupled to the underlying $PtSe_2$ lattice.

In our Zn–air systems, Hu *et al.* and Feng *et al.* demonstrated that dielectric-barrier discharge (DBD) and RF plasma treatment of NiFe/$NiSe_2$ and CoNiSe-based air cathodes induces the formation of non-stoichiometric surface layers rich in oxygen vacancies or selenium vacancies, along with modulated metal valence states (*e.g.*, Ni^{2+}/Ni^{3+}, Co^{2+}/Co^{3+}) and enhanced electronic conductivity.[56,57] These structural and electronic modifications lead to improved ORR/OER activities, higher limiting current densities, lower overpotentials, and superior cycling stability in both liquid and flexible all-solid-state Zn–air batteries. These works underscore that plasma-induced vacancy engineering is a universal strategy for enhancing the performance of chalcogenide-based electrocatalysts, analogous to its role in oxides.

In many cases, defects and interfaces are generated together, and their interplay becomes the dominant control knob for activity. Zhang *et al.* provide a representative CoP_3/Ni_2P example, where an Ar microwave plasma treatment targets the ultrathin 2D heterostructure and drives interfacial P escape, generating P-vacancy defects preferentially at the CoP_3/Ni_2P junction[13] (Fig. 5b). Meanwhile, a fraction of these vacancies is occupied by external oxygen to form O-refilling defects, producing a mixed defective interface rather than a single clean junction. Such vacancy-decorated heterointerfaces reconstruct the local electronic structure, intensify charge redistribution across Co- and Ni-centred sites, and lower kinetic barriers – thereby enhancing HER *via* improved H* binding and promoting alkaline steps by facilitating interfacial charge transfer and water activation.

Similar defect-rich heterojunctions arise in our Co-based Zn–air catalysts after plasma activation, where Co/CoO, Co–N–C and carbon nanotube frameworks are intimately coupled, as reported by Xiong *et al.*[23] (Fig. 5c). Here, an oxygen RF plasma was used to activate the air electrode, because O-containing radicals/ions can introduce oxygen non-stoichiometry and interfacial disorder without the thermal budget that would sinter Co-based sites or collapse the CNT network. In these systems, plasmas introduce vacancies and disordered coordination at the metal/oxide or metal/carbon interfaces, leading to enhanced electronic coupling and more favorable ORR/OER kinetics at the composite level rather than at any single phase in isolation.

Taken together, these studies show that plasma-induced defects are not random damage but structured design elements. Oxygen, chalcogen and pnictogen vacancies, coordination distortions, defect-rich interfaces and ultrathin disordered shells all arise from the same basic features of non-thermal plasmas: a flux of energetic electrons and reactive radicals that act within only a few surface layers, far from thermodynamic equilibrium. The resulting defect ensembles tune metal valence, introduce new electronic states, increase covalency in metal–ligand bonds and redistribute charge across junctions, thereby modulating the adsorption and transformation of key intermediates in HER, OER, ORR and CO_2 reduction. In combination with the phase transformation pathways discussed

earlier, plasma defect engineering therefore provides an orthogonal yet synergistic handle for reprogramming surface chemistry and electronic landscapes.

2.3. Plasma-induced doping and surface functionalization

Low-temperature plasmas provide a third mode of control over electrocatalysts beyond phase transformation and vacancy creation: they can selectively introduce heteroatoms into the near-surface region and thereby rewrite the local electronic structure without sacrificing the underlying phase or nanoarchitecture. Unlike bulk doping achieved by high-temperature diffusion or solution-based routes, plasma-induced doping is inherently shallow and interface-focused, enabling controlled modification of surface electronic structure without altering the bulk composition. Energetic electrons and reactive radicals act within only a few nanometers, breaking specific metal–ligand or C–C bonds and creating transient open sites that can be occupied by N, F, P, B or oxygenated fragments. This section discusses plasma enabled incorporation of heteroatoms or functional groups, identified by composition changes and bonding motifs related signatures.

A first, and perhaps clearest, manifestation of this behavior is seen in N/F doping of transition-metal oxides and chalcogenides, where the primary role of plasma is to tune the covalency and energy alignment of metal–ligand bonds. Li *et al.* used an NH_4F-containing RF plasma to co-introduce N and F into Co_3O_4 nanowire arrays while preserving the spinel phase and 1D architecture[4] (Fig. 6a). The key outcome is electronic: dual anion incorporation strengthens Co–O covalency and shifts the O 2p band closer to the Fermi level, lowering the barrier for lattice-oxygen participation and pushing OER from a purely adsorbate-evolution route toward a more lattice-oxygen-involved pathway, without changing the nanowire backbone. Density functional calculations corroborate that dual N, F incorporation pulls the O 2p band closer to the Fermi level and increases Co–O covalency, which lowers the free-energy barrier for lattice-oxygen participation.

Plasma-enabled N doping can also be used to construct multi-parameter surface motifs, in which heteroatoms, vacancies and even metastable phases cooperate. Zheng *et al.* treated MoS_2 with RF NH_3 plasma to produce N-doped, vacancy-rich and partially 1T-phase MoS_2 for tandem plasma–electrocatalytic nitrogen chemistry[8] (Fig. 6b and c) The plasma step introduces N into the S sublattice, creates S vacancies and induces a local 2H to 1T transition, again confined to the near-surface region. Calculations show that these features collectively enhance charge transfer to nitrogenous intermediates and suppress hydrogen evolution by shifting the Mo d states and creating electron-rich traps at N/S-defective sites. In this case, the dopant is not a passive spectator but an integral part of a complex defect-phase ensemble, yet the macroscopic morphology of the MoS_2 support is preserved.

Analogous principles apply in carbon-based systems. Li *et al.* exposed quasi-graphene to N_2 plasma, introducing pyridinic, pyrrolic and graphitic nitrogen into the topmost carbon layers while retaining the overall sheet-like morphology[16] (Fig. 6d). The nitrogen functionalities increase the density of edge-like sites, improve electronic conductivity and adjust the redox potential of surface carbon atoms, which together translate into markedly enhanced peroxidase-mimicking activity towards H_2O_2. Here, the active phase is the doped carbon itself rather than a transition metal, but the underlying logic is the same: plasma-installed N dopants and associated defects reshape the local density of states at the Fermi level and create chemically distinct adsorption sites, without the need for high-temperature bulk treatments.

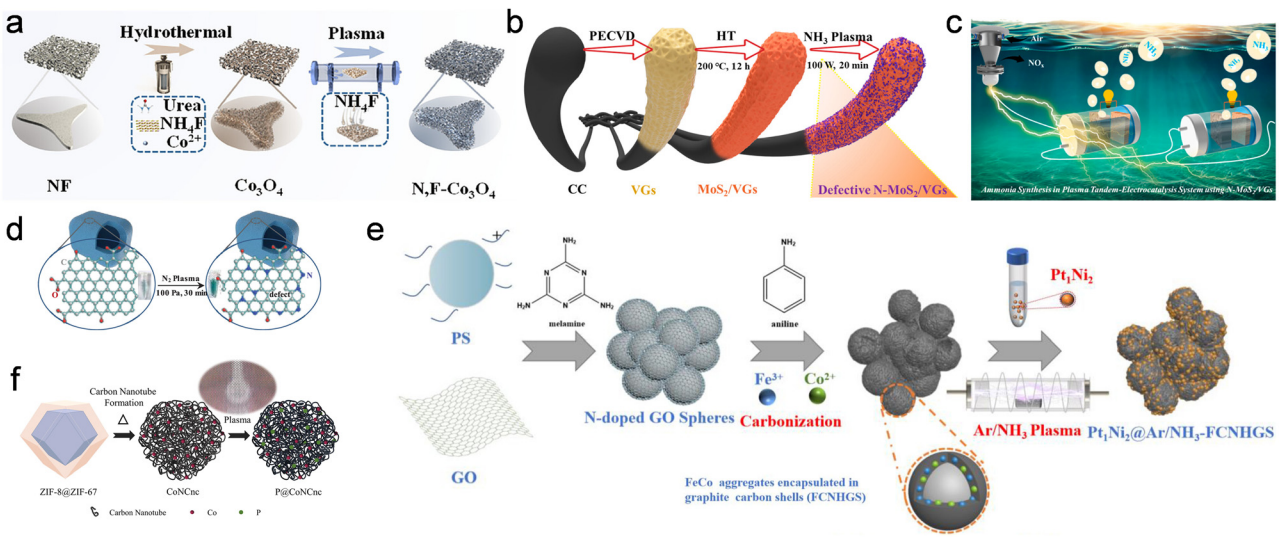

Fig. 6 (a) Schematic illustration of the synthesis process of the N,F-Co_3O_4. Reproduced with permission.[4] Copyright 2025, Wiley-VCH. (b) Schematic illustration for N-MoS_2/VGs engraved by RF NH_3 plasma. (c) The plasma tandem-electrolysis system. Reproduced under the terms of CC-BY 4.0 license.[8,9] (d) Schematic illustration showing the synthesis of N-doped quasi-graphene by N_2 Plasma. Reproduced with permission.[16] Copyright 2020, American Chemical Society. (e) Illustration of the fabrication of Pt_1Ni_2@Ar/NH_3-FCNHGS. Reproduced with permission.[29] Copyright 2023, Elsevier. (f) Schematic showing the P soft doping of CoNCnc by microwave plasma. Reproduced with permission.[34] Copyright 2025, Elsevier.

Within our own work, Gong *et al.* used atmosphere-programmed plasma to tune N doping and defect density in Fe/Co/N-decorated hollow graphene spheres as supports for $PtNi_2$ nanoparticles[29] (Fig. 6e). The source is an RF plasma operated at low pressure, allowing the reactive environment to be switched simply by changing the feed gas. Among the atmospheres, Ar/NH_3 is the most effective because it couples Ar-driven etching with NH_x chemistry: OES shows NH- and H-related species during discharge, consistent with simultaneous surface roughening/defect creation and the formation of pyridinic/graphitic N and Fe(Co)–N_x motifs. These N-rich defects act as anchoring sites that suppress $PtNi_2$ agglomeration and strengthen metal–support electronic coupling, as reflected by the binding-energy shifts of Pt and Ni. The resulting catalysts deliver improved ORR/HER activity and fuel-cell durability compared with undoped or thermally doped counterparts, highlighting plasma N-doping as a practical route to engineer carbon supports for higher noble-metal utilization.

In many plasma-treated systems, doping is intimately coupled to defect formation so that vacancies act as entry points for heteroatoms. This vacancy-mediated route provides a natural bridge between the defect engineering discussed earlier and the doping strategies considered here. In the $NiCo_2O_4$ study by Zheng *et al.*[58] DBD plasma first generates abundant oxygen vacancies in the spinel lattice, partially reducing Co^{3+} to Co^{2+} and disordering the local Co–O environment. Subsequent nitrogen incorporation occurs preferentially at these defective sites, forming Ni–N_x and Co–N_x coordinations that stabilize the vacancies and further modify the electronic structure. A similar sequence arises in the NiCoP system of Zhang *et al.*, where vacuum annealing and plasma treatment create oxygen-deficient $NiCoO_x$ precursors, and N doping during phosphidation yields an N-doped, vacancy-rich NiCoP surface.[59] In both cases, dopants and vacancies form coupled ensembles: vacancies lower the barrier for substitution, and the heteroatoms in turn stabilize and electronically activate the defective sites.

Huang *et al.* reached a related conclusion in N, Fe co-incorporated CoO nanoarrays: the N, Fe co-bonded CoO was formed *via* a nitrogen-plasma step carried out in a N_2 PECVD reactor, and the reactive nitrogen species (*e.g.*, N/excited N_2/N_2^+) generated in the discharge both etch the surface and enable near-surface N incorporation. As a result, N acts as a chemical bridge to bind Fe and Co centers while simultaneously promoting oxygen non-stoichiometry and higher-valent Co at the surface, pointing to a cooperative adjustment of vacancies, dopants and metal valence that optimizes the energetics of lattice-oxygen-involved OER.[60]

Beyond directly modifying active phases, plasma doping can be applied in a ''soft'' fashion to carbon and interfacial layers, where the principal outcome is to re-engineer metal–support interactions, wettability and charge-transfer pathways rather than bulk band structure. Ai *et al.* used a microwave plasma to gently dope phosphorus into Co nanoparticle-embedded, nest-like N-doped carbon frameworks[34] (Fig. 6f). Mechanistically, energetic electrons in the microwave discharge volatilize the phosphate salt into short-lived P-containing radicals/ions ($P^*/PO_x/PH_x^*$), which graft onto defected carbon and Co–N sites to form covalent P–C and P–O–C motifs. The P functionalities introduce additional defects, increase hydrophilicity and adjust the local electron density around Co–N centers, leading to improved oxygen reduction activity and stability compared with undoped samples. Lin *et al.* employed oxygen plasma to activate carbon nanotube-interconnected Prussian blue analogue nanoarrays.[61] The treatment decorates CNTs with oxygenated groups and partially oxidizes the PBA surface, thereby lowering interfacial resistance and introducing more redox-active metal–oxygen moieties for the OER.

Zhao *et al.* show that plasma is useful not just as a ''doping step'', but as a sequence controller for building multi-heteroatom interfaces in porous carbon/NiFe hybrids for zinc–air batteries.[62] An initial Ar plasma etch activates the carbon scaffold – creating defects and opening access to embedded NiFe domains – so that subsequent B doping and NH_3 treatment can be directed to the most reactive carbon sites and, critically, to the metal–support boundary. The outcome is a coupled B/N environment (B–C, B–O and interfacial M–N_x motifs) in which plasma-created defects act as nucleation/anchoring points, stabilizing high-valent Ni/Fe centers while improving charge transport through the porous carbon network. As a result, the co-doped architecture delivers stronger ORR/OER bifunctionality and improved zinc–air cell performance than singly doped or undoped counterparts, underscoring plasma's value as a practical platform for constructing electronically synergistic interfaces rather than isolated dopant sites.

Taken together, these studies demonstrate that plasma-induced dopants are not random impurities but precisely placed design elements that operate alongside phases and vacancies. In the N/F-doped oxides and chalcogenides, heteroatoms directly tune metal–ligand covalency and shift band positions, thereby optimizing the adsorption energies of key intermediates in OER, ORR and nitrogen reduction. In vacancy-assisted systems, dopants and defects are co-localized, with vacancies enabling heteroatom incorporation and the heteroatoms stabilizing and electronically activating the defective sites. In soft-doped carbons and interfacial layers, heteroatoms such as N, P and B reshape metal–support interactions, wettability and local charge distributions, improving utilization and stability of the catalytically active phase. Across all cases, the distinctive advantage of non-thermal plasmas lies in their ability to sculpt these dopant landscapes within only a few surface layers, far from thermodynamic equilibrium and without sacrificing the integrity of carefully designed nanoarchitectures. In combination with the phase-transformation and defect-engineering pathways discussed earlier, plasma-enabled doping thus provides a complementary and highly versatile lever for reprogramming surface chemistry and electronic structure in electrocatalysts.

2.4. Deposition and interface engineering

Plasma processing does more than transform bulk phases or create vacancies; it actively constructs the interfacial landscape through which electrons, ions and molecules exchange. This section highlights cases where plasma is used to deposit,

reduce, or assemble a secondary component and the main outcome is a designed junction or conformal coating, tracked by dispersion, thickness, and interfacial electronic fingerprints. Compared with wet-chemical deposition or thermal growth, plasma-enabled deposition allows reactive species to be delivered directly to the surface under non-equilibrium conditions, facilitating the construction of ultrathin interfaces and heterostructures without prolonged thermal exposure. In many representative systems, plasma acts simultaneously as a surface activator and a non-thermal driver for metal nucleation, enabling catalytic metals or secondary phases to be anchored onto predesigned architectures with interfacial chemistries that are purposefully engineered rather than incidentally formed.

Li *et al.* illustrated this using Pt-decorated $NiCo_2O_4$ nanowire arrays for bifunctional oxygen electrocatalysis and Zn–air batteries.[63] Specifically, a RF Ar plasma is used to activate the oxide mainly through energetic Ar^+ bombardment/electron-stimulated oxygen removal, followed by a brief H_2/Ar plasma that supplies $H^{\bullet}/e^-$ for rapid *in situ* reduction of Pt precursors and immediate interfacial anchoring. Compared with thermal treatment, the plasma route produces smaller and more uniformly dispersed Pt domains and strengthens the Pt–$NiCo_2O_4$ interfacial interaction. These features lower the charge-transfer resistance and enhance ORR/OER kinetics, consistent with stronger electronic coupling at the Pt–oxide interface that optimizes oxygen-intermediate binding rather than simply increasing Pt loading.

A similar interplay between deposition and interface activation appears across a family of plasma-engineered fuel-cell electrodes. In the work by Zha *et al.*, PtNi nanoparticles were assembled on nitrogen-doped carbon nanotubes (NCFs) grown from CoFe-layered double hydroxide precursors, using Ar/NH_3 RF plasma treatment.[64] The plasma served to create defects and oxygen vacancies in the carbon support, enhance PtNi loading, and reduce the oxidation state of Pt and Ni, leading to improved catalytic activity for both ORR and MOR in alkaline direct methanol fuel cells. Hu *et al.* combined RF Ar/H_2 plasma pretreatment of N-doped carbon nanotubes with plasma reduction of Pt precursors, showing that defects introduced into the carbon framework provide high-affinity anchoring sites and that plasma reduction yields Pt nanoparticles with an optimized fraction of oxidized surface atoms.[65] Wang *et al.* used direct-current plasma magnetron sputtering to deposit an ultralow loading of Pt onto self-standing CoFe@NCNT electrodes, achieving uniform coverage along the nanotube array and excellent trifunctional activity[7] (Fig. 7a). Across these examples, the role of the plasma is not limited to "putting metal onto a support"; it prepares specific chemical and topological anchoring sites, suppresses agglomeration and constructs extended metal–support contact networks, so that noble metals are wired into conductive oxide or carbon scaffolds with minimal dead surface.

Plasmas can also deposit or trigger the growth of oxide shells that are electronically coupled to their underlying metallic or mixed-metal cores. In our group's DMFC work and in related Zn–air systems, short plasma exposures convert the outer layers of transition-metal sulfides, nitrides or carbons

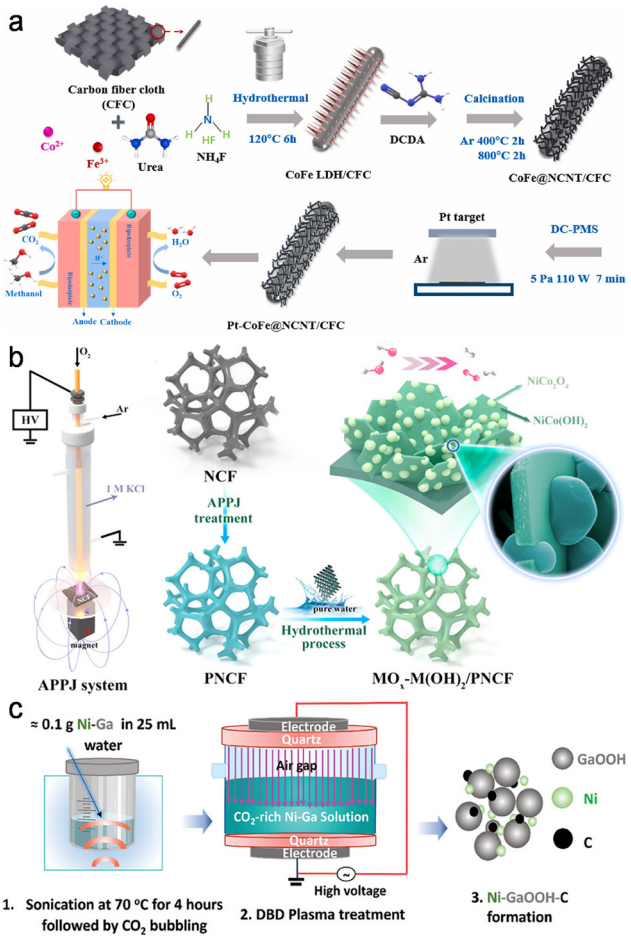

Fig. 7 (a) Schematic illustration of the synthesis process of Pt-CoFe@NCNT/CFC electrode. Reproduced with permission.[7] Copyright 2022, Elsevier. (b) The schematic illustration for the fabrication of the electrode-emerged nanointerfaced bimetallic NiCo hydroxide–oxide active system. Reproduced with permission.[19] Copyright 2021, American Chemical Society. (c) Schematic showing the synthesis of Ni-GaOOH-C catalyst. Reproduced under the terms of CC-BY 4.0 license.[24]

into thin, defective oxides while preserving the inner phase. When noble metals or additional functional phases are subsequently deposited, they sit on top of an electronically active oxide interlayer rather than directly on the parent phase. In this stacked structure, the deposited metal, the plasma-formed oxide layer and the conductive core work together to generate internal potential gradients and redox-buffer regions that enhance charge separation and stabilize high-valent states under operating conditions. The interfacial chemistry is again set by the plasma: its radicals and ions determine how deeply oxidation proceeds, which cations are oxidized and how many vacancies or hydroxyl groups remain to bind the next layer.

Another group of studies uses plasmas to fabricate or modify non-noble catalytic films and their junctions with light absorbers or conductive backbones. Benedet *et al.* employed PECVD to grow three-dimensional, flower-like MnO_2 nanoarchitectures on Ni foam and then coupled them with g-C_3N_4 *via* electrophoretic deposition (EPD), forming an extended oxide/semiconductor junction for photo-assisted OER. The plasma controls both the

Mn oxidation state and the film porosity, ensuring that the g-C_3N_4 flakes contact a defect-rich MnO_2 surface rather than a compact, poorly hydrated oxide.[66] Chen *et al.* developed a ''plasma-triggered growth'' route to fabricate NiCo hydroxide–oxide nanointerfaces directly on nickel foam[19] (Fig. 7b). In this case, the plasma first oxidizes and roughens the metal surface; exposure to water then drives spontaneous growth of intertwined $NiCo(OH)_x/NiCo_2O_4$ domains. The resulting interpenetrating hydroxide/oxide network exhibits fast redox kinetics and enhanced charge storage, highlighting how plasma-triggered surface chemistry can be harnessed to grow nanointerfaces directly from a current collector without separate precursors or binders. They first applied a magnetically focused atmospheric-pressure plasma jet in an Ar/O_2 mixture to locally activate the NiCo foam surface. Subsequent immersion/hydrothermal treatment in pure water without added reagents then drives the electrode to ''sprout'' intertwined $NiCo(OH)_x$ nanosheets that are densely decorated with strongly bonded NiCo oxide nanoparticles, yielding an interpenetrating hydroxide/oxide network with fast redox kinetics and robust high-current overall water-splitting performance.

Babikir *et al.* extended this interfacial thinking to liquid-metal-derived Ni–Ga system, where a dielectric barrier discharge plasma reduces dissolved CO_2 into highly dispersed activated carbon that deposits directly onto *in situ*-formed Ni–GaOOH particles[24] (Fig. 7c). The resulting material is not merely ''Ni–GaOOH plus carbon'' but a tightly intergrown Ni–O–C region containing metallic Ni, NiO_x and graphitic carbon domains. DFT shows that the Ni–C and NiO_x–C interfaces significantly lower the free-energy barriers for nitrate reduction to ammonia relative to either Ni or NiO alone, indicating that the plasma-generated carbon phase constructs the true ensemble of active interfacial sites. Deas *et al.* demonstrated a related concept for WO_{3-x} films produced by aerosol-assisted atmospheric-pressure plasma jets: pre-formed oxide colloids are assembled into hierarchical, porous layers whose internal grain boundaries, necks and pore walls are fused by the plasma.[67] Even without additional metals, the resulting network has a high density of electrically connected internal interfaces that facilitate charge percolation and ion access, underscoring that ''deposition'' in a plasma context often means welding together a three-dimensional interfacial scaffold rather than laying down a flat film.

At still thinner length scales, PEALD offers atomic-level control over interfacial composition and wetting. Hoek *et al.* compared plasma-enhanced and purely thermal ALD of In_2S_3 thin films on gas-diffusion electrodes for CO_2 electroreduction.[68] The plasma process produces films with different surface terminations, defect densities and wettability, which in turn tune the gas–liquid–solid triple-phase boundary and stabilize high formate partial current densities. In a similar research, Li *et al.* used plasma to engineer Pt–O–W interfaces on tungsten-based supports at extremely low Pt loadings.[69] The plasma not only reduces Pt precursors but also creates oxygen-bridged Pt–O–W linkages at the contact region, modifying the local electronic structure so that hydrogen adsorption and desorption kinetics are optimized for HER. In both cases, the key advantage of the plasma is its ability to set the chemical identity and polarity of just a few atomic layers at the interface – whether by controlling ligand terminations in ALD cycles or by forming specific metal–oxygen–metal bridges – while leaving the bulk of the support untouched.

Taken together, these deposition and interfacial studies show that non-thermal plasmas are effective tools for producing catalytic junctions directly onto three-dimensional scaffolds. Noble metals can be anchored as ultrasmall particles at plasma-generated defect sites on oxides or carbons; oxide and oxyhydroxide shells can be grown from plasma-activated surfaces; carbon or chalcogenide domains can be nucleated *in situ* on oxide backbones; and atomic-scale junctions can be defined through PEALD or plasma-driven ligand chemistry. In all of these cases, the active region is not a single phase, but a thin, chemically complex interfacial zone where electronic coupling, local fields and wetting properties are all set by the preceding plasma exposure. Because these modifications are confined to the outer few nanometers, the underlying nanoarchitecture continues to provide mechanical support and long-range charge and mass transport. When viewed alongside the phase and defect engineering routes discussed earlier, plasma-assisted deposition and interfacial design complete a coherent picture in which low-temperature plasmas are used to sculpt not only what phases are present, but also how they touch and communicate, thereby controlling where the true catalytic work is done.

2.5. Single atom anchoring and strong interactions

In the previous sections we have seen how plasmas can reshape phases, inject defects, introduce heteroatoms and sculpt interfaces. A natural end point of this evolution is the regime where these structural motifs no longer act independently but instead lock into one another through strong electronic interactions and atomically precise coordination. In this regime, the catalytically relevant unit is no longer a ''particle on a support'' but a coupled ensemble of vacancies, single atoms, clusters and oxide frameworks whose behavior is defined by interfacial charge redistribution. This section addresses plasma strategies that stabilize atomically dispersed metals or strongly coupled metal support contacts, supported by single atom evidence from HAADF STEM or EXAFS and by clear interfacial charge transfer or enhanced stability under operation. Relative to conventional impregnation or high-temperature anchoring strategies, non-thermal plasma is particularly effective at creating surface-confined anchoring sites and strong metal–support interactions, stabilizing single atoms and interfacial charge transfer motifs under electrochemical operating conditions.

A recurring theme across several systems is that plasma first creates or reorganizes anion vacancies, which then serve as chemically selective anchoring sites for isolated metals. In the Pt/TiO_{2-x} single-atom catalyst reported by Tian *et al.*, alternate plasma sputtering was used to deposit Pt atoms on a pre-deposited TiO_{2-x} support[5] (Fig. 8a). The TiO_{2-x} support contained a low concentration of Ti^{3+} and oxygen vacancies, which, together with the Pt–O coordination, helped stabilize Pt in a linear O–Pt–O configuration, prevent aggregation, and enhance

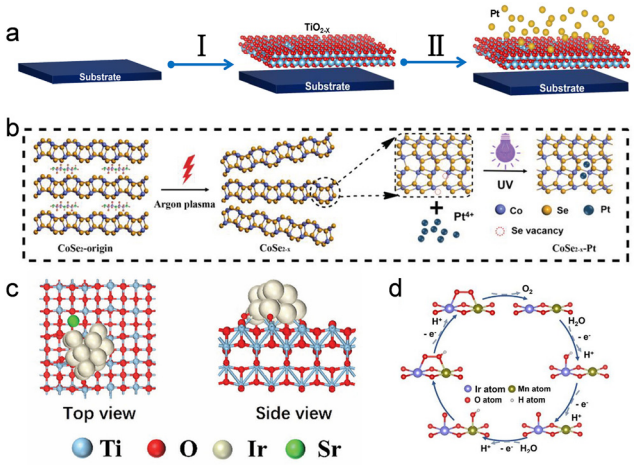

Fig. 8 (a) Schematic illustration of the synthesis process of the Pt/TiO_{2-x} catalyst. Reproduced with permission.[5] Copyright 2021, Elsevier. (b) Schematic of the Ar-plasma-induced exfoliation of $CoSe_2$-origin. Reproduced with permission.[18] Copyright 2018, Wiley-VCH. (c) Top and side views of Ir@Sr-d-TiO_2(004). Reproduced with permission.[22] Copyright 2024, Wiley-VCH. (d) OER process by the IMO@p-ATO through OPM. Reproduced with permission.[33] Copyright 2025, Wiley-VCH.

electron transfer. This resulted in a catalyst with ultra-low Pt loading (1.69 wt%) that outperformed commercial Pt/C in mass activity and TOF for the HER. A similar vacancy-templated strategy underlies the Pt–Co–Se coordinated sites in $CoSe_2$ described by Zhuang *et al.*: Ar plasma generates Se vacancies that, during subsequent photochemical reduction, guide Pt into well-defined Pt–Co–Se configurations with highly asymmetric charge distribution and lowered barriers for key OER intermediates[18] (Fig. 8b). In a more complex perovskite host, Han *et al.* showed that plasma-enhanced CVD simultaneously induces A-site deficiency in $LaFeO_3$ and drives Ru incorporation, yielding a mixed population of Ru single atoms and Ru clusters embedded in the lattice.[70] Operando analysis indicates that these two Ru species communicate through the perovskite oxygen network, jointly sustaining high N_2 reduction rates. In all three cases, the plasma step does more than "activate" a surface: it writes a vacancy landscape that dictates where and how single atoms and clusters are stabilized, and how they subsequently talk to the support.

Once these anchoring environments are in place, the interaction between metal and host often enters the strong metal–support interaction (SMSI) regime, in which charge transfer and orbital hybridization become as important as geometric confinement. A mechanistic template for such behavior is provided by Pt/NbO_x in the work of Jia *et al.*, where the Pt–NbO_x interface switches between Pt–O and Pt–Nb coordination depending on oxygen coverage, yet in all cases electrons flow from Pt into the oxide.[71] This electron depletion stabilizes low-coordinated Pt sites, contracts Pt–Pt bonds and suppresses dissolution under ORR conditions. Plasma-engineered systems map naturally onto this picture. In the Ir/TiO_2 nanowire catalyst of Zhu *et al.*, H_2/N_2 plasma first generates oxygen-vacancy-rich TiO_2, which tightly anchors Ir nanoparticles; the vacancy-rich skin also enforces strong interfacial electronic coupling, so that Ir is stabilized by a more polar/ionic metal–oxide contact rather than weak physisorption[22] (Fig. 8c). These V_O sites further act as preferred adsorption/coordination traps for the Sr promoter, making the subsequent Sr single-atom introduction spatially correlated with the Ir–oxide contact region. Sr single atoms are then introduced at or near these vacancies. The resulting Ir–Sr–TiO_2 triple interface shows pronounced charge redistribution in theory, stabilizes high-valent Ir–O intermediates in experiment, and dramatically reduces Ir loss during acidic OER/HER and PEM electrolysis.

In a carbon-based analogue, Yi *et al.* used N_2 plasma to introduce pyridinic and graphitic N into graphene, which then form Ir–N coordination shells around ultra-small Ir particles.[72] The associated negative shift in Ir binding energy and enhanced durability point again to a SMSI-like electronic coupling: the plasma-modified support donates and redistributes charge in a way that optimizes adsorbate binding and protects the noble metal.

These material-specific examples can be viewed through a broader conceptual lens. Zhou *et al.* has argued that in oxide electrocatalysts, strong oxide–support interactions (SOSI) and defect–interface coupling drive interfacial electronic reconstruction: shifting the O 2p band center, modulating M–O covalency and steering the balance between adsorbate evolution mechanisms and lattice oxygen pathways[33] (Fig. 8d). Vacancy-rich suboxide skins, heteroatom-decorated carbon shells and perovskite lattices populated by embedded clusters and single atoms all fit naturally into this SOSI/SMSI framework. What plasma processing adds is a kinetic shortcut to such states: it can simultaneously create vacancies, reduce or partially oxidize metals, and install single-atom promoters in the same near-surface region, thereby collapsing multi-step wet-chemical protocols into a single, controllable interface-writing operation.

Taken together, the systems illustrate how non-thermal plasmas can be used not only to disperse metals, but to sculpt the interaction landscape around them. By designing vacancy types and densities, choosing supports capable of SOSI/SMSI behavior, and judiciously adding single-atom promoters, it becomes possible to assemble interfacial motifs in which geometry, valence and reaction pathway are co-determined. This perspective suggests that future progress in plasma-assisted electrocatalysis will depend less on pushing any single lever – phase, defect, doping or interface – in isolation, and more on deliberately integrating the strong, atom-scale interactions that emerge when all of these levers are pulled together.

3. Conclusions

The design logic of electrocatalysts with non-thermal plasma is straightforward. One first selects a scaffold that is worth preserving – oxide nanowires, MOF-derived carbons, carbon textiles, or pre-grown chalcogenide sheets – so that the bulk architecture continues to provide electronic and mass-transport pathways. The plasma discharge is then used to place an appropriate phase at the surface: phosphides to combine metallic conduction with

optimized H* binding, nitrides to provide conductivity and charge-transfer support, and vacancy-rich chalcogenides or sub-oxides to tune the chemistry of oxygen intermediates. The conversion layer is kept thin so that internal interfaces are dense while transport through the backbone remains fast. When precious metals are required, plasma activation can be exploited to generate anchoring defects, followed by a brief plasma reduction or sputtering step to control dispersion and oxidation state, thereby improving utilization and stability. Where strong interactions are desired, defect-rich skins are combined with subsequent metal loading or single-atom decoration so that charge transfer and coordination environments are established from the outset and preserved under electrochemical load.

Equally important are the limits and common pitfalls. Not every system benefit from deeper penetration; beyond the first few nanometers, gains in active area are often offset by increased resistance, poorer wetting, or accumulated mechanical stress. Morphology collapse can occur if gas heating or exposure times are excessive, and is best avoided by modest power, short treatment steps and, when necessary, cooling flows. Non-thermal plasma processing is inherently surface-confined and therefore not suited for bulk modification, and its effectiveness depends on well-defined process windows. As such, plasma should be regarded as a complementary interface-engineering tool rather than a universal substitute for conventional materials processing methods. Robust recipes arise when process variables are explicitly correlated with surface composition and structure, and these in turn are linked to kinetic response, allowing those relationships to be condensed into simple and reproducible operating windows. To support this point, Table 1 was provided that collates representative plasma parameters, structural fingerprints and catalytic metrics, helping readers identify reproducible processing windows across systems.

Looking ahead, the most important opportunities lie in tightening the loop between plasma physics, surface structure and electrochemical function. *Operando* spectroscopy and microscopy, coupled with realistic modelling of non-thermal discharges at catalyst interfaces, will be essential to follow how plasma-written phases, defects and strong interactions evolve under current and potential. At the same time, translating these ideas beyond model electrodes to porous gas-diffusion layers, membrane–electrode assemblies and large-area electrodes will require closer integration of reactor design, diagnostics and device testing. If these threads can be woven together, non-thermal plasmas should move from being occasional activation steps to becoming genuinely predictive tools for constructing robust, low-PGM electrodes, with the active chemistry written exactly where the electrochemical work is done.

Author contributions

Chu Qin: conceptualization; investigation; visualization; writing – original draft; writing – review and editing. Zhenglong Tao: investigation; data curation; resources; writing – review and editing. Xuanhao Wu: supervision; writing – review and editing. Zhongqing Jiang: supervision; project administration; writing – review and editing.

Conflicts of interest

There are no conflicts to declare.

Data availability

No primary research results, software or code have been included, and no new data were generated or analyzed as part of this review.

Acknowledgements

Authors acknowledge the supports from the National Natural Science Foundation of China (No. 12505288, 12275239, and 52400098), the Zhejiang Provincial Natural Science Foundation (No. QN26A050005, LR22E070001, and LZ25B070003).

Notes and references

1 Z. Xu, J. Wu, W. Chen, Z. Jiang, J. Cao, G. Chen and Z.-J. Jiang, *Adv. Funct. Mater.*, 2025, e11117.
2 L. Xu, Q. Jiang, Z. Xiao, X. Li, J. Huo, S. Wang and L. Dai, *Angew. Chem., Int. Ed.*, 2016, **55**, 5277–5281.
3 D. Zha, R. Wang, S. Tian, Z.-J. Jiang, Z. Xu, C. Qin, X. Tian and Z. Jiang, *Nano-Micro Lett.*, 2024, **16**, 250.
4 C. Li, B. Ye, B. Ouyang, T. Zhang, T. Tang, Z. Qiu, S. Li, Y. Li, R. Chen, W. Wen, M. Song, B. Mei, X. Xia and Y. Zhang, *Adv. Mater.*, 2025, **37**, 2501381.
5 Y. Tian, L. Yu, C. Zhuang, G. Zhang and S. Sun, *Mater. Today Energy*, 2021, **22**, 100877.
6 L. Wang, J. Qi, Y. Zhang, Y. Dai, K. Bao, W. Wang, J. Wu, C. Ma, Z. Yin, C. Ma, Y. Chen, J. Bao, R. Ye, Y. Liu, Z. Lin, Z. Wang and Q. He, *Adv. Mater.*, 2025, **37**, 2502047.
7 W. Wang, Z. Jiang, X. Tian, T. Maiyalagan and Z.-J. Jiang, *Carbon*, 2023, **201**, 1068–1080.
8 J. Zheng, H. Zhang, J. Lv, M. Zhang, J. Wan, N. Gerrits, A. Wu, B. Lan, W. Wang, S. Wang, X. Tu, A. Bogaerts and X. Li, *J. Am. Chem. Soc. Au*, 2023, **3**, 1328–1336.
9 J. Huang, H. Sheng, R. D. Ross, J. Han, X. Wang, B. Song and S. Jin, *Nat. Commun.*, 2021, **12**, 3036.
10 H. Liang, A. N. Gandi, C. Xia, M. N. Hedhili, D. H. Anjum, U. Schwingenschlögl and H. N. Alshareef, *ACS Energy Lett.*, 2017, **2**, 1035–1042.
11 Z. Shao, Q. Zhu, Y. Sun, Y. Zhang, Y. Jiang, S. Deng, W. Zhang, K. Huang and S. Feng, *Adv. Mater.*, 2022, **34**, 2110172.
12 X. Wu, X. Wang, Y. Wu, H. Xu, Z. Li, R. Hong, K. Rigby, Z. Wu and J.-H. Kim, *Nat. Commun.*, 2025, **16**, 1122.
13 L. Zhang, L. Zhuang, H. Liu, L. Zhang, R. Cai, N. Chen, X. Yang, Z. Zhu, D. Yang and X. Yao, *Small Science*, 2021, **1**, 2000027.
14 B. Ouyang, Y. Zhang, X. Wang, Y. Deng, F. Liu, Z. Fang, R. S. Rawat and E. Kan, *Small*, 2022, **18**, 2204634.
15 K. E. Salem, A. A. Saleh, G. E. Khedr, B. S. Shaheen and N. K. Allam, *Energy Environ. Mater.*, 2023, **6**, e12324.
16 S. Li, X. Zhao, R. Gang, B. Cao and H. Wang, *Anal. Chem.*, 2020, **92**, 5152–5157.
17 H. Han, S. Jin, S. Park, Y. Kim, D. Jang, M. H. Seo and W. B. Kim, *Nano Energy*, 2021, **79**, 105492.
18 L. Zhuang, Y. Jia, H. Liu, X. Wang, R. K. Hocking, H. Liu, J. Chen, L. Ge, L. Zhang, M. Li, C.-L. Dong, Y.-C. Huang, S. Shen, D. Yang, Z. Zhu and X. Yao, *Adv. Mater.*, 2019, **31**, 1805581.
19 G. Chen, D. Chen, J. Huang, C. Zhang, W. Chen, T. Li, B. Huang, T. Shao, J. Li and K. K. Ostrikov, *ACS Appl. Mater. Interfaces*, 2021, **13**, 45566–45577.

20 X. Li, H. Jiang, C. Ma, Z. Zhu, X. Song, H. Wang, P. Huo and X. Li, *Appl. Catal., B*, 2021, **283**, 119638.
21 L. Ye, W. Chen, Z. J. Jiang and Z. Jiang, *Carbon Energy*, 2024, **6**, e457.
22 H. Zhu, Y. Wang, Z. Jiang, B. Deng, Y. Xin and Z.-J. Jiang, *Adv. Energy Mater.*, 2024, **14**, 2303987.
23 Y. Xiong, Z. Jiang, L. Gong, X. Tian, C. Song, T. Maiyalagan and Z.-J. Jiang, *J. Colloid Interface Sci.*, 2023, **649**, 36–48.
24 A. H. Babikir, X. Mao, A. Du, J. D. Riches, K. Ostrikov and A. P. O'Mullane, *Small*, 2024, **20**, 2311302.
25 B. Ouyang, S. Peng, H. Qin, Y. Du, J. Xu, Y. Cao, E. Kan and R. S. Rawat, *Appl. Catal., B*, 2025, **366**, 125061.
26 K. Huang, D. Peng, Z. Yao, J. Xia, B. Zhang, H. Liu, Z. Chen, F. Wu, J. Wu and Y. Huang, *Chem. Eng. J.*, 2021, **425**, 131533.
27 X. Yan, L. Zhuang, Z. Zhu and X. Yao, *Nanoscale*, 2021, **13**, 3327–3345.
28 M. Li, X. Wang, K. Liu, H. Sun, D. Sun, K. Huang, Y. Tang, W. Xing, H. Li and G. Fu, *Adv. Mater.*, 2023, **35**, 2302462.
29 L. Gong, Z. Jiang, Y. Xiong, X. Tian and Z.-J. Jiang, *Int. J. Hydrogen Energy*, 2023, **48**, 32860–32874.
30 H. Song, J. Yu, Z. Tang, B. Yang and S. Lu, *Adv. Energy Mater.*, 2022, **12**, 2102573.
31 J. Fan, L. K. Arrazolo, J. Du, H. Xu, S. Fang, Y. Liu, Z. Wu, J.-H. Kim and X. Wu, *Environ. Sci. Technol.*, 2024, **58**, 12823–12845.
32 C. Qin, S. Tian, J. Wu, J. Mou, L. Feng and Z. Jiang, *ChemCatChem*, 2024, **16**, e202401033.
33 K. Zhou, Y. Wang, Z. Jiang, B. Dai and Z.-J. Jiang, *Adv. Mater.*, 2025, **37**, 2420159.
34 J. Ai, N. Wang, F. Li, W. He, Z. Qu, X. Ma, L. Huang and Q. Pu, *Appl. Surf. Sci.*, 2025, **688**, 162448.
35 K. Fan, H. Zou, Y. Lu, H. Chen, F. Li, J. Liu, L. Sun, L. Tong, M. F. Toney, M. Sui and J. Yu, *ACS Nano*, 2018, **12**, 12369–12379.
36 M. Zhang, Q. Dai, H. Zheng, M. Chen and L. Dai, *Adv. Mater.*, 2018, **30**, 1705431.
37 X. Wang, L. R. Winter, X. Wu, Y. Fan, Y. Zhao, J.-H. Kim and M. Elimelech, *Sci. Adv.*, 2025, **11**, eads6943.
38 L. Li, X. Tang, B. Wu, B. Huang, K. Yuan and Y. Chen, *Adv. Mater.*, 2024, **36**, 2308326.
39 K. Chen, S. Kim, M. Je, H. Choi, Z. Shi, N. Vladimir, K. H. Kim and O. L. Li, *Nano-Micro Lett.*, 2021, **13**, 60.
40 J.-Y. Kim, M.-J. Jin, B. Hou, M. P. Kim, D.-S. Um and C.-I. Kim, *Appl. Surf. Sci.*, 2023, **639**, 158271.
41 T. Zhang, J. Wu, J. Chen, Q. Pan, X. Wang, H. Zhong, R. Tao, J. Yan, Y. Hu, X. Ye, C. Chen and J. Chen, *ACS Appl. Mater. Interfaces*, 2021, **13**, 24682–24691.
42 S. Song, M. Guo, S. Zhang, K. Zhan, Y. Yan, J. Yang, B. Zhao and M. Xu, *Electrochim. Acta*, 2020, **331**, 135431.
43 R. Wang, Z. Guo, X. Tan, J. Zhang, L. Yang, W. Wang, L. Cao and B. Dong, *Int. J. Hydrogen Energy*, 2021, **46**, 32425–32434.
44 F. Yu, M. Liu, C. Ma, L. Di, B. Dai and L. Zhang, *Nanomaterials*, 2019, **9**, 1436.
45 G. Li, X. Wu, H. Guo, Y. Guo, H. Chen, Y. Wu, J. Zheng and X. Li, *ACS Appl. Mater. Interfaces*, 2020, **12**, 5951–5957.
46 Y. Liu, Z. Jiang and Z.-J. Jiang, *Adv. Funct. Mater.*, 2023, **33**, 2302883.
47 H. Liu, S. Jiang, J. Li, W. Chen, Z.-J. Jiang, X. Tian and Z. Jiang, *Small*, 2025, **21**, 2504987.
48 Y. Wei, L. Yi, S. Zhang, C. Ni, X. Cai, W. Sun and W. Hu, *J. Mater. Chem. A*, 2024, **12**, 8534–8542.
49 Z. Fu, Z. Jiang, T. Hu and Z.-J. Jiang, *Electrochim. Acta*, 2022, **419**, 140392.
50 B. Zhang, Z. Jiang, X. Shang, S. Li and Z.-J. Jiang, *J. Mater. Chem. A*, 2021, **9**, 25934–25943.
51 J. Zhang, W. Nie, R. Wang, C. Qin, Z.-J. Jiang, G.-R. Jin and Z. Jiang, *J. Alloys Compd.*, 2024, **1004**, 175900.
52 J. Mallmann, J.-B. Chemin, D. Cardenas Morcoso, A.-M. Philippe, S. Bulou, N. Chaabane, F. Rouillard, P. Choquet and N. D. Boscher, *ACS Appl. Energy Mater.*, 2025, **8**, 7038–7051.
53 G. Yang, H. Xiang, M. Rauf, H. Mi, X. Ren, P. Zhang and Y. Li, *J. Power Sources*, 2021, **481**, 228925.
54 H. Liang, Z. Cao, C. Xia, F. Ming, W. Zhang, A.-H. Emwas, L. Cavallo and H. N. Alshareef, *CCS Chem.*, 2021, **3**, 1553–1561.
55 B. Zhang, X. Shang, Z. Jiang, C. Song, T. Maiyalagan and Z.-J. Jiang, *ACS Appl. Energy Mater.*, 2021, **4**, 5059–5069.
56 T. Hu, Z. Jiang, Z. Fu and Z.-J. Jiang, *J. Mater. Chem. A*, 2022, **10**, 8739–8750.
57 Y. e Feng, W. Chen, L. Zhao, Z. J. Jiang, X. Tian and Z. Jiang, *Small Methods*, 2024, **8**, 2400565.
58 J. Zheng, X. Peng and Z. Wang, *Phys. Chem. Chem. Phys.*, 2021, **23**, 6591–6599.
59 Y. Zhang, Z. Zhu, X. Guo, J. Qi and X. Li, *Chem. Eng. J.*, 2023, **452**, 139230.
60 K. Huang, Y. Yan, Y. Yu, T. Yang, L. Qiao, J. Tu, J. Sui, W. Cai, S. Liu and X. Zheng, *EES Catal.*, 2025, **3**, 1044–1054.
61 Y.-C. Lin, C.-H. Chuang, L.-Y. Hsiao, M.-H. Yeh and K.-C. Ho, *ACS Appl. Mater. Interfaces*, 2020, **12**, 42634–42643.
62 L. Zhao, J. Zhang, G. Jin, Z.-J. Jiang and Z. Jiang, *J. Colloid Interface Sci.*, 2024, **668**, 525–539.
63 H. Li, L. Hansen, A. Aliyeva, J. Wang, H. Qiu, M. Müller, S. Chen, C. Aktas, L. Kienle, B. Hartke and J. Benedikt, *Appl. Catal., B*, 2025, **361**, 124607.
64 D. Zha, S. Jiang, Q. Zhang, J. Li, Z.-J. Jiang, C. Qin, X. Tian, T. Maiyalagan and Z. Jiang, *Chem. Eng. J.*, 2025, **522**, 166892.
65 T. Hu, W. Chen, Y. Liu, L. Gong, Z. Jiang, D. Bhalothia, T. Maiyalagan and Z.-J. Jiang, *Small*, 2023, **19**, 2304076.
66 M. Benedet, A. Gallo, C. Maccato, G. A. Rizzi, D. Barreca, O. I. Lebedev, E. Modin, R. McGlynn, D. Mariotti and A. Gasparotto, *ACS Appl. Mater. Interfaces*, 2023, **15**, 47368–47380.
67 R. Deas, T. Lolohea, A. Chan, G. I. N. Waterhouse, G. Henshaw, D. J. McGillivray and D. E. Williams, *ACS Appl. Nano Mater.*, 2023, **6**, 5613–5622.
68 J. Van den Hoek, F. Mathew, L. Hintjens, B. De Coen, E. Solano, M. M. Minjauw, R. Blomme, N. Daems, D. Choukroun, C. Detavernier, J. Dendooven and T. Breugelmans, *Adv. Energy Mater.*, 2025, **15**, 2404178.
69 J. Li, Q. Zhang, H. Liu, Z.-J. Jiang, X. Tian and Z. Jiang, *Appl. Phys. Lett.*, 2025, **127**, 203903.
70 Z. Han, D. Tranca, F. Rodríguez-Hernández, K. Jiang, J. Zhang, M. He, F. Wang, S. Han, P. Wu and X. Zhuang, *Small*, 2023, **19**, 2208102.
71 Q. Jia, S. Ghoshal, J. Li, W. Liang, G. Meng, H. Che, S. Zhang, Z.-F. Ma and S. Mukerjee, *J. Am. Chem. Soc.*, 2017, **139**, 7893–7903.
72 L. Yi, B. Feng, N. Chen, W. Li, J. Li, C. Fang, Y. Yao and W. Hu, *Chem. Eng. J.*, 2021, **415**, 129034.

